PROCEEDINGS, 41st Workshop on Geothermal Reservoir Engineering
Stanford University, Stanford, California, February 22-24, 2016
SGP-TR-209

High Temperature Hydrothermal Metamorphism at The Geysers Geothermal Field, California: An Investigation of Mineral Chemistry and Vein Paragenesis from an Active Contact Metamorphic Environment

Clay Jones[1,2], Joseph Moore[1], John Bowman[2] and Mark Walters[3]

[1]Energy & Geoscience Institute at the University of Utah, Salt Lake City UT
[2]University of Utah Geology and Geophysics Department, Salt Lake City UT
[3]Calpine Corporation, Middletown CA
cjones@egi.utah.edu

Keywords: mineral chemistry, vein mineral paragenesis, electron microprobe, scanning electron microscopy, petrography, hydrothermal alteration, contact metamorphism.

ABSTRACT

Core samples from eight deep wells in The Geysers geothermal field that define a transect from the intrusive core of the system through the contact metamorphosed Franciscan metagraywacke and argillite that hosts the high temperature vapor dominated geothermal reservoir have been examined by electron microprobe, scanning electron and petrographic microscopic techniques to document mineral chemistries and vein paragenesis.

Vein paragenesis in the suite of core samples shows early veins of: biotite + apatite + quartz + pyrite ± plagioclase ± pyrite ± ilmenite; tourmaline + quartz + chlorite ± K-feldspar ± plagioclase ± epidote ± titanite ± pyrite ± ilmenite ± chalcopyrite; and actinolite + plagioclase + apatite + quartz + pyrite. With later: epidote + quartz + K-feldspar + plagioclase ± actinolite ± chlorite ± chalcopyrite ± pyrite ± ilmenite ± prehnite ± wairakite; and K-feldspar ± pyrite ± titanite.

Three hundred and sixty-six electron microprobe analyses of vein and wall rock mineral chemistries have been collected from: biotite (seventy-seven); tourmaline (one hundred and sixteen); calcic amphibole (twenty); apatite (thirty-three); plagioclase (fourteen); epidote (thirty-one); chlorite (forty-three); titanite (eight); and K-feldspar (twenty-five). Biotite chemistry data from veins and contact metamorphic wall rock were collected from two cores. The biotite is annite to phologopite in composition with Mg/(Mg+Fe) values ranging from 0.37 to 0.56 and Al contents ranging from 1.12 to 1.62 apfu with overlapping compositional ranges. Variations in Mg, Fe, Al and Cl content were observed between vein and wall rock biotite and disparities in F content were observed between the two cores with average F contents of 0.20 and 0.02 apfu. Vein and wall rock tourmaline chemistry data was collected from four cores. Tourmaline is dominantly foititc to scholitic in composition with less abundant dravitic species. All tourmaline measurements fall into the alkali and X-site vacant groups. No systematic zoning was observed in relation to distance from the pluton, but zoning within crystals was observed, from base to tip in elongated grains, and within adjacent domains of sector zoned tourmalines. Comparison of tourmaline in the contact metamorphic wall rock to vein tourmaline from the same core showed that vein tourmaline is enriched in Al and F. Vein calcic amphibole chemistry data was collected from one core and was found to be actinolite to magnesiohornblende in composition. Apatite chemistry data was collected from two cores. The monovalent anion site showed variable composition between cores and at the grain scale, ranging between nearly end member F and OH apatite species in one core to OH-rich apatite with minor Cl (< 0.26 apfu) and negligible F in another. Plagioclase was observed in one core as Ca-rich (average An_{75}) vein selvages. Epidote from veins within the intrusive contained low abundances of rare earth elements (Ce < 0.17, Nd < 0.06, La < 0.11 apfu), but no relationship between Al and Fe^{+3} content and distance from the intrusive was observed. Chlorite chemistry data was collected from five cores and is dominantly clinochlore in composition with less abundant chamosite. Chlorite is found in veins across the entire core transect, from within the intrusive, out into the geothermal reservoir and shows a trend of increasing Mg content with distance from the intrusive with Mg/(Mg+Fe) values ranging from 0.11 to 0.60. Vein titanite chemistry was collected from two cores and was found to be Al- and F-rich with average Al and F contents of 0.39 and 0.27 apfu respectively.

1. INTRODUCTION

The Geysers geothermal field is located in the Mayacmas Mountains, roughly 150 km north of San Francisco, California on the southeastern edge of the larger Pliocene to Holocene Clear Lake volcanic field (Donnelly-Nolan et al., 1993). The Geysers is the largest producer of geothermal energy in the world (720 MWe; Moore and Simmons, 2014), and is notable as being one of only a handful of vapor-dominated geothermal systems. Water-rock interactions within the hydrothermal system and have increased the strength of the country rocks, allowing them to support low pressure vapor-static steam filled fractures at depth. Understanding the mechanisms, extent and spatial variability of the alteration in the fracture networks and country rock will aid in future exploration and development of both the conventional and Enhanced Geothermal System reservoirs at The Geysers.

The geothermal reservoir at The Geysers covers an area of approximately 160 km^2 (Walters and Coombs, 1989) and is hosted within the fractured and contact metamorphosed metasediments of the Mesozoic Franciscan Complex and to a lesser degree the underlying plutonic rocks. The Franciscan Complex was metamorphosed to subgreenschist facies and locally to blueschist facies conditions during accretion of the Franciscan to the Pacific plate (McNitt, 1968; McLaughlin, 1981; Thompson, 1989). Highly convoluted veins of quartz and calcite are a common feature of the regional metamorphism (McNitt, 1968; McLaughlin, 1981; Sternfeld, 1981). Within The

Geysers geothermal system, dissolution of the calcite in these deformed veins has created porosity for the deposition of hydrothermal minerals (Moore and Gunderson, 1995).

Volcanic activity (basaltic andesite followed by more voluminous rhyodacite) in The Geysers-Clear Lake area began at about 2.1 Ma, continuing intermittently with the most recent eruption occurring at 0.01 Ma (Donnelly-Nolan et al., 1981). Accompanying intrusive igneous activity may have begun as early as 2.5 Ma (Schriener and Suemnicht, 1981). The pluton underlying The Geysers is informally referred to as the felsite. It has been intersected at depths as shallow as 700 m below the surface and has a volume in excess of 300 km^3 at an elevation above 4,400 mbsl (Donnelly-Nolan et al., 1993; Norton and Hulen, 2001). It is elongated in a northwest-southeast orientation (Figure 1), subparallel to the regional faults (Hulen and Norton, 2000). Regional NW-SE trending strike-slip faults related to San Andreas faulting have affected both the Mesozoic Franciscan complex and the geometry of the intrusion at The Geysers. Seismic evidence (Bufe et al., 1981; Oppenheimer, 1986) indicates that The Geysers-Clear Lake area is currently under extensional stress.

The felsite is composed of at least three intrusive bodies. The oldest is a biotite microgranite porphyry that forms the shallow cupola of the pluton. U-Pb dating of zircon has yielded an age of 1.76 ± 0.01 Ma (Schmitt et al., 2002). Younger intrusive bodies include an orthopyroxene-biotite granite and a hornblende-pyroxene-biotite granodiorite. U-Pb analyses of zircon and $^{40}Ar/^{39}Ar$ age spectra suggest these units were emplaced between 1.13 ± 0.06 and 1.28 ± 0.01 Ma, respectively (Dalrymple et al., 1999; Schmitt et al., 2002). Several younger rhyolite dikes have been encountered in geothermal well bores. One has yielded a $^{40}Ar/^{39}Ar$ total-fusion age of 0.57 Ma (Pulka, 1991); another a U-Pb zircon age of 1.13 ± 0.04 Ma (Schmitt et al., 2002).

It has been suggested that intrusion ages of less than 1 Ma are too old to account for the high reservoir temperatures observed at The Geysers today (Walters and Combs, 1992; Williams et al., 1993; Dalrymple et al., 1999; Norton and Hulen, 2001; Schmitt et al., 2002). To account for the prolonged heating at The Geysers, either a large long-lived magma chamber (Isherwood, 1981; McLaughlin, 1981), or incremental intrusions of smaller, as yet undetected plutons must be present (Stanley and Blakely, 1995; Stanley et al., 1998). One such young intrusive body may lie beneath the northwestern portion of the field. Core from deep wells in this area provide samples of contact metamorphosed rock (biotite hornfels), but intrusive rocks have not been encountered. Evidence for a recent intrusion in this area includes measured temperatures as high as 400°C (Lutz et al., 2012); steep conductive temperature gradients of up to 50°C/100m (Walters et al., 1988); high $^{3}He/^{4}He$ ratios in the steam (Torgerson and Jenkins, 1982; Kennedy and Truesdell, 1996); and high HCl contents of the steam (Truesdell et al., 1989; Lowenstern and Janick, 2003). Heat flow data suggest that igneous activity could have occurred as recently as 5,000 to 10,000 years ago in the northwest Geysers (Williams et al., 1993).

Mineral assemblages related to contact metamorphism and hydrothermal alteration are concentrically zoned around the pluton and are linked to the emplacement of the felsite (Thompson and Gunderson, 1989; Sternfeld, 1989; Hulen et al., 1991, 1992; Moore and Gunderson, 1995; Norton and Hulen, 2001; Lutz et al., 2012). A contact metamorphic aureole forms a rind around the intrusive 300 to >600 m thick. The contact metamorphosed rock is a biotite hornfels characterized by disseminated biotite and veins or vug fillings in dissolution cavities containing tourmaline and/or biotite (Moore and Gunderson, 1995).

Mineralogic, fluid inclusion and isotopic studies record the evolution of the geothermal system from an early liquid-dominated hydrothermal system to the present-day vapor-dominated regime (Moore and Gunderson, 1995; Moore et al., 2000). The vapor-dominated regime developed when discharge exceeded recharge through the low permeability rocks surrounding the system (White et al., 1971; Truesdell and White, 1973). Chalcedony overgrowths on quartz and the common occurrence of vapor-rich fluid inclusions throughout the field suggest the transition from liquid- to vapor-dominated conditions was accompanied by widespread, and possibly catastrophic boiling (Moore et al., 2000).

The current vapor-dominated regime consists of two reservoirs, the high temperature vapor-dominated reservoir (HTVDR) and the normal temperature vapor-dominated reservoir (NVDR) (Drenick, 1986; Walters et al., 1988). The HTVDR lies below the NVDR in the northwest portion of the field where the youngest intrusive is suspected to be concealed. Temperature and pressure measurements made prior to production indicate that the NVDR had a temperature of ~240°C and a pressure of ~35 bars (vaporstatic) that remained constant with depth. In the northwestern portion of the field measured temperatures of up to 400°C and pressures only marginally higher than in the overlying NVDR have been encountered, suggesting the HTVDR and NVDR are hydraulically connected (Walters et al., 1988; Lutz et al., 2012). Steep temperature gradients up to 50°C/100 m have been observed between the two reservoirs (Walters et al., 1988). Based on fluid inclusion data indicating that boiling occurred in the temperature range of 330° to 240°C (Moore et al., 2000), $^{40}Ar/^{39}Ar$ spectrum dating on hydrothermal adularia (0.57 ± 0.03 Ma at 300-330°C) (Hulen et al., 1997) and thermal modeling (Dalrymple et al., 1999) It has been postulated that the transition from liquid- to vapor-dominated conditions occurred between 0.28 and 0.25 Ma (Hulen et al., 1997).

Despite the considerable amount of petrologic work characterizing the hydrothermal alteration at The Geysers little is known about the chemistry of the alteration minerals. In this study, core samples from eight wells that define a transect from the intrusive through the surrounding biotite hornfels and the HTVDR reservoir have been investigated using petrographic, scanning electron microscope and electron microprobe techniques. The chemical data supplement previous descriptions of the vein paragenesis by Moore and Gunderson (1995) and Hulen (1991). This paper presents the initial results of the chemical analyses.

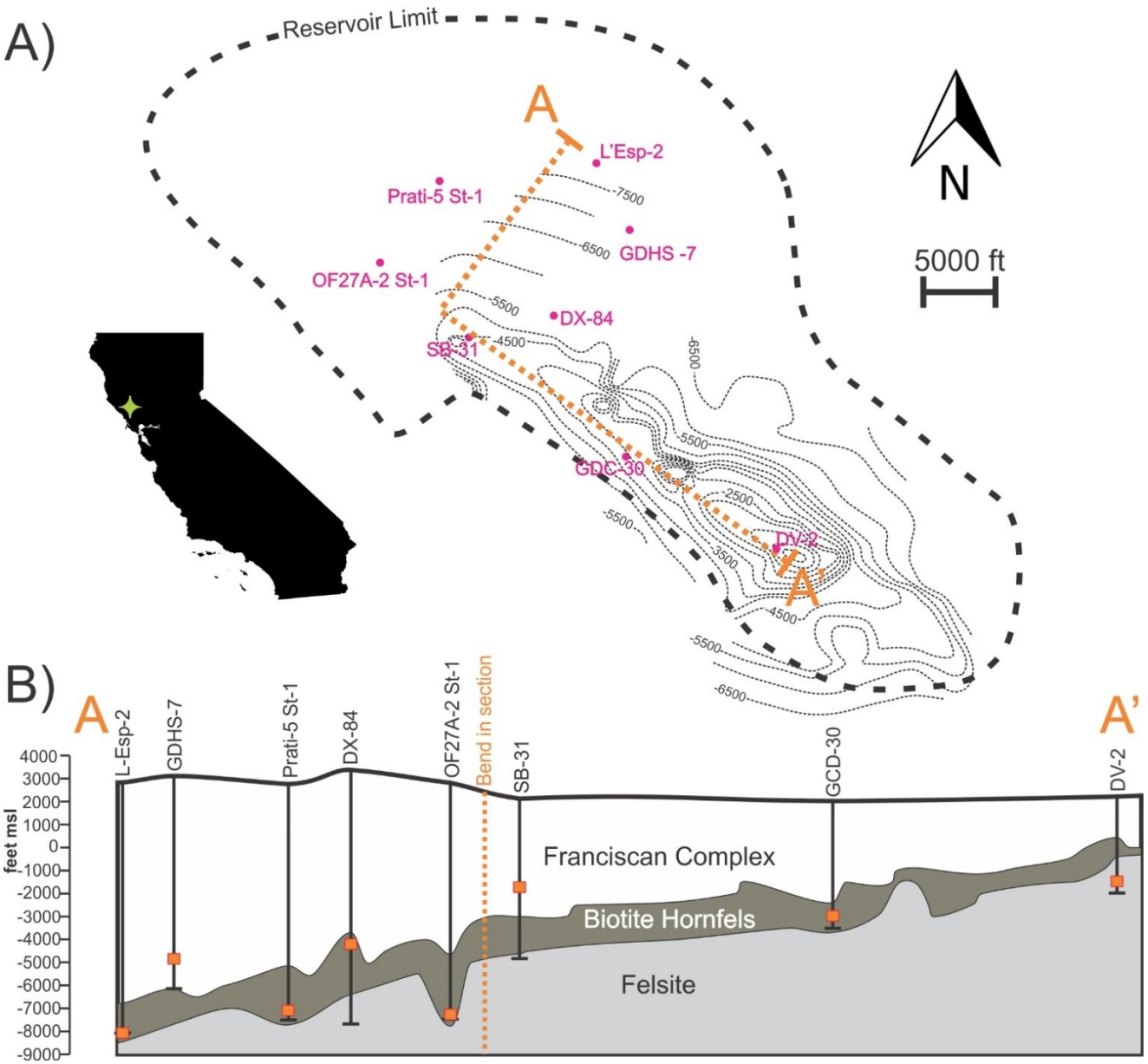

Figure 1: A) Contour map of the top of The Geysers pluton (felsite) at 500 ft increments relative to mean sea level. Locations of wells with cored intervals selected for this study are shown in pink. B) Simplified cross-section of The Geysers geothermal field (orange section line shown in A) with cored intervals shown in red and orange. Deviated wells are shown as vertical with cored intervals and total depths converted from measured depth to true vertical depth. Top of hornfels map courtesy of Calpine.

2. METHODS

2.1 Scanning electron microscopy

Scanning electron microscopy was conducted at the Energy & Geoscience Institute using a JEOL IT-300 scanning electron microscope (SEM) equipped with a Deben Centaurus cathodoluminescence (CL) detector and an Oxford X-act energy dispersive detector (EDS). Backscatter electron (BSE) photomosaic images of entire thin sections were generated to guide electron microprobe analyses. BSE, EDS and CL were used as preliminary tools to identify minerals, assess paragenetic relationships, and investigate chemical variations within individual mineral grains and as a function of the distance from the intrusion.

2.2 Electron microprobe

Wave length dispersive spectroscopy was conducted at the University of Utah Geology and Geophysics department using a Cameca SX-50 electron microprobe (EMP) equipped with four wavelength dispersive X-ray spectrometers. Under nominal operating conditions, typical detections limits are 300 ppm and precision for major elements in on the order of 1% of the amount present. Spot sizes ranged from 10 to 5 µm. An accelerating voltage of 15 kV and current of 30 nA were used. Count times were 10 seconds off peak and 20 seconds on peak for all elements with the exception of F. For F, count times were 20 seconds off peak and 40 seconds on peak. As a

precaution, F was analyzed first in an effort to minimize F migration under the electron beam. EMP data does not include information on oxidation states or analyses of light elements such as B, H and Li.

3. PARAGENESES

In addition to the polished thin sections made for this study a suite of thin sections housed at the Energy & Geoscience Institute core library have been examined to determine the vein mineral paragenesis in the eight wells selected for study. A sub set of six samples from five of these wells has been examined in detail using SEM and EMP methods to evaluate the vein mineral paragenesis and characterize the chemistry of the vein minerals. Observed vein paragenetic relationships are documented in figures 2 and 3.

The paragenesis of veins at The Geysers has been previously described by Moore and Gunderson, (1995) and Hulen (1991). The veins are spatially and temporally zoned around the intrusive body. Veins within the felsite and the biotite hornfels contain tourmaline ± biotite ± actinolite ± clinopyroxene ± epidote + quartz + K-feldspar or biotite ± tourmaline ± actinolite ± clinopyroxene ± epidote + quartz + K-feldspar (paragenesis 1). With increasing distance from the intrusive contact, the vein assemblages are characterized by actinolite ± epidote ± ferroaxinite ± prehnite ± titanite + quartz + K-feldspar (paragenesis 2); epidote ± chlorite ± titanite + quartz + K-feldspar (paragenesis 3); quartz + K-feldspar ± calcite ± epidote ± prehnite ± sulfides ± chlorite (paragenesis 4a); and quartz (or chalcedony) ± calcite ± chlorite ± sericite ± wairakite (paragenesis 4b).

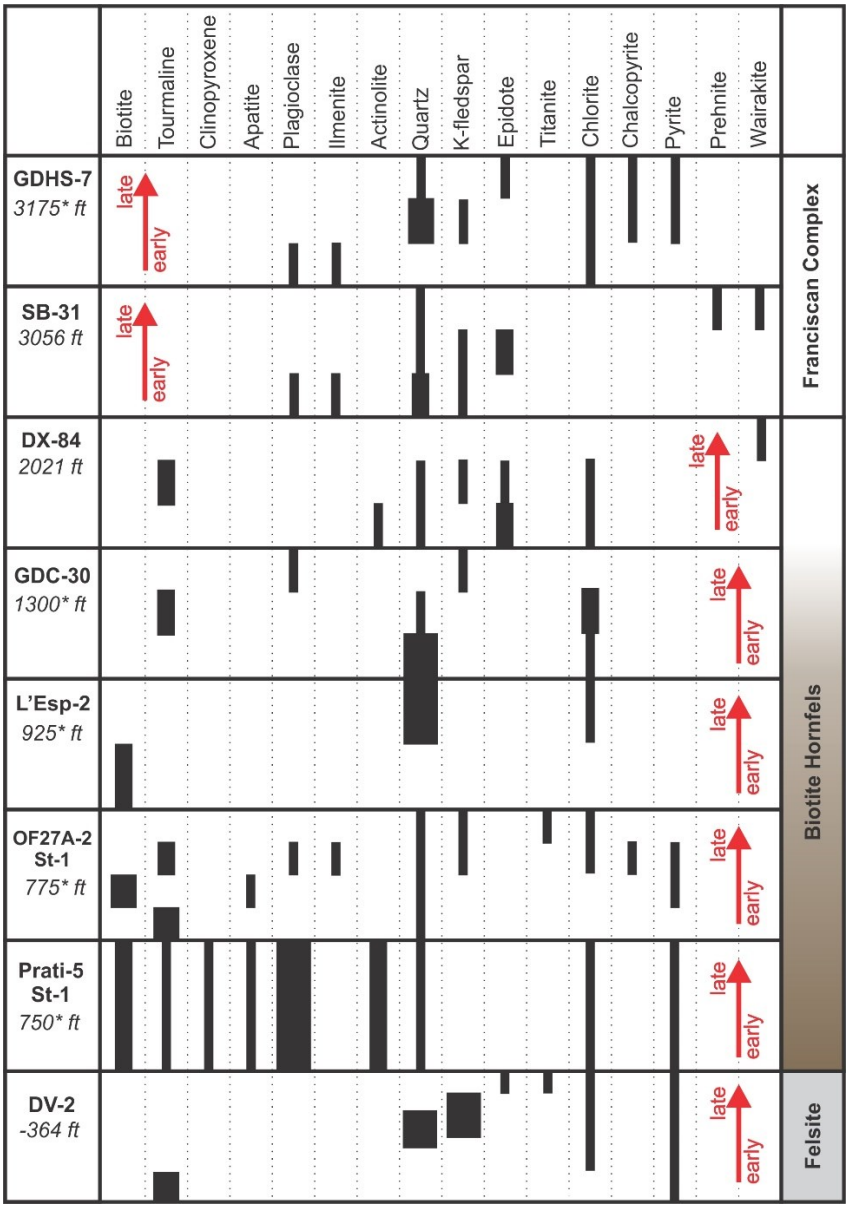

Figure 2: Observed vein paragenetic relationships in the eight core samples studied supplemented with data from Hulen (1991) and Lutz et al. (2012). Wells are arranged from top to bottom with respect to distance to the felsite. An * adjacent to the footages on the left indicates exact distances are uncertain. The lithology of the vein host is shown on the right. Relative vein mineral abundances are indicated by the thickness of the black bars. The red arrows show the progression of vein mineral deposition from early (bottom) to late (top) for each core sample.

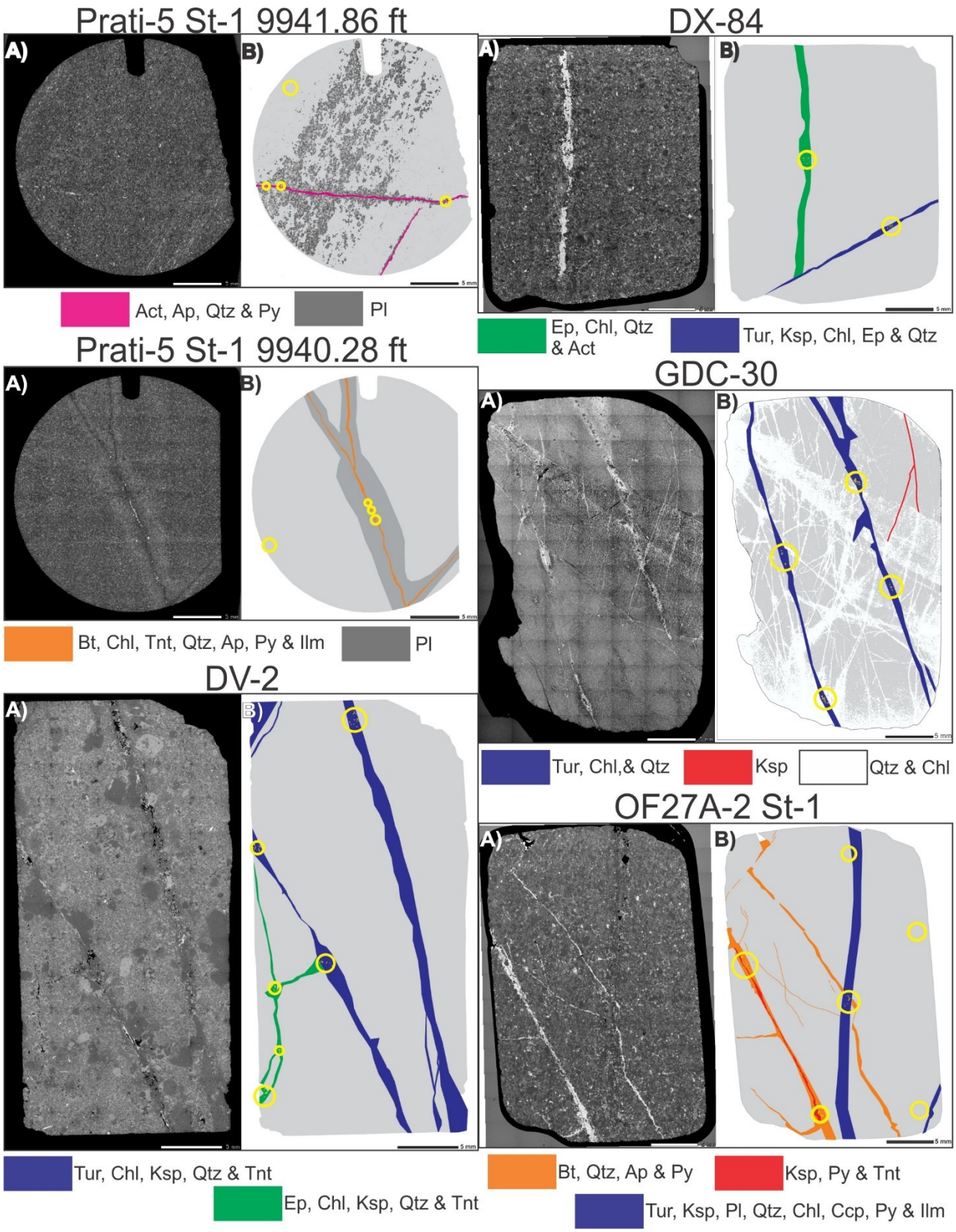

Figure 3: Polished sections of core samples that have been selected for EMP analyses showing veins and areas where EMP data points were acquired. A) BSE SEM photomosaics of thin sections. B) Simplified views of the polished sections with veins and vein selvages highlighted. Veins and selvages are color coded to the legend at the bottom of each image. Yellow circles indicate areas where EMP analyses were collected. Abbreviations used in this figure: Act = actinolite; Ap = apatite; Bt = biotite; Ccp = chalcopyrite; Chl = Chlorite, Ep = epidote; Ilm = ilmenite; Ksp = K-feldspar; Pl = plagioclase; Py = pyrite; Qtz = quartz; Tnt = titanite; Tur = tourmaline. All scale bars = 5 mm.

3.1 Paragenesis 1

The earliest formed veins belong to paragenesis 1. These veins contain biotite + apatite + quartz + pyrite ± plagioclase ± pyrite ± ilmenite; tourmaline + quartz + chlorite ± K-feldspar ± plagioclase ± epidote ± titanite ± pyrite ± ilmenite ± chalcopyrite; and actinolite + plagioclase + apatite + quartz + pyrite.

3.1.1 Biotite

EMP chemical data of vein biotite and biotite from the biotite hornfels wall rock was obtained from core samples OF27A-2 St-1 and Prati-5 St-1 (Figure 4). Twenty-nine analyses were collected from OF27A-2 St-1 (twenty-two vein, seven wall rock) an additional twenty-two legacy analyses furnished by Calpine are incorporated into the data set (seventy-seven total biotite analyses). Twenty-six biotite analyses were collected from Prati-5 St-1 (fourteen vein, twelve wall rock). In OF27A-2 St-1 the biotite bearing veins also contained apatite, quartz and pyrite. In Prati-5 St-1 vein biotite is partially altered to chlorite (Figure 5) and occurs with apatite, titanite, quartz, pyrite and ilmenite. In addition, the biotite veins in Prati-5 St-1 have Ca-rich plagioclase vein selvages. Vein biotite that has been extensively replaced by quartz, chlorite and titanite was also observed in L'Esp-2, but the very small regions (micron scale) of unaltered biotite were not suitable for EMP analyses. Raw EMP data and calculated formulas of representative biotite analyses can be found in the appendix.

Biotite structural formulas were calculated from EMP data based on an eleven oxygen per formula unit basis. All Fe was assumed to be Fe^{2+}. Biotite has a general formula of $K(Fe,Mg)_3AlSi_3O_{10}(OH)_2$. Biotite compositions from both cores are broadly similar and plot primarily in the annite field with less abundant phologopite (Figure 4). Vacancies observed in the large cation site ranged from 0 to 0.17 atoms per formula unit (apfu) with an average of 0.06 apfu. Octahedral sites had vacancies that ranged from 0.0 to 0.18 apfu with an average of 0.01 apfu. F and Cl were detected in the monovalent anion site at up to 0.48 and 0.32 apfu, respectively.

In OF27A-2 St-1 biotite in the contact metamorphosed rock matrix is similar in composition to vein biotite, with less compositional variability observed in the wall rock biotite. The vein biotite is enriched in Fe compared to the wall rock biotite. The Cl and F content of the monovalent anion site are also fairly similar in the veins and rock matrix. The Cl content of the vein and wall rock biotite average 0.18 and 0.22 apfu respectively, with wall rock biotite slightly enriched in Cl. The F content of the vein and wall rock biotite average 0.23 and 0.15 apfu, respectively, with vein biotite enriched in F.

In Prati-5 St-1 vein biotite is depleted in Al and Mg compared to biotite within the biotite hornfels wall rock. Biotite from both the wall rock and veins have low average F contents of 0.02 and 0.01 apfu respectively. The Cl content of vein biotite and wall rock biotite average of 0.34 and 0.13 apfu respectively, with vein biotite enriched in Cl. Biotite from Prati-5 St-1 contained significantly less F than OF27A-2 St-1.

Compositional differences between biotite and their chlorite replacements from Prati-5 St-1 are shown in figure 5. Biotite has slightly higher Mg/(Mg+Fe) than chlorite. Chlorite is enriched in Al, Fe and Mg and is depleted in K, Cl, F and Ti compared to biotite. The Si content of biotite and chlorite are similar. EMP analyses of secondary chlorite show low abundances of K, Ca and Ti, most likely resulting from remnant biotite layers intercalated with the secondary chlorite and fine-grained secondary titanite.

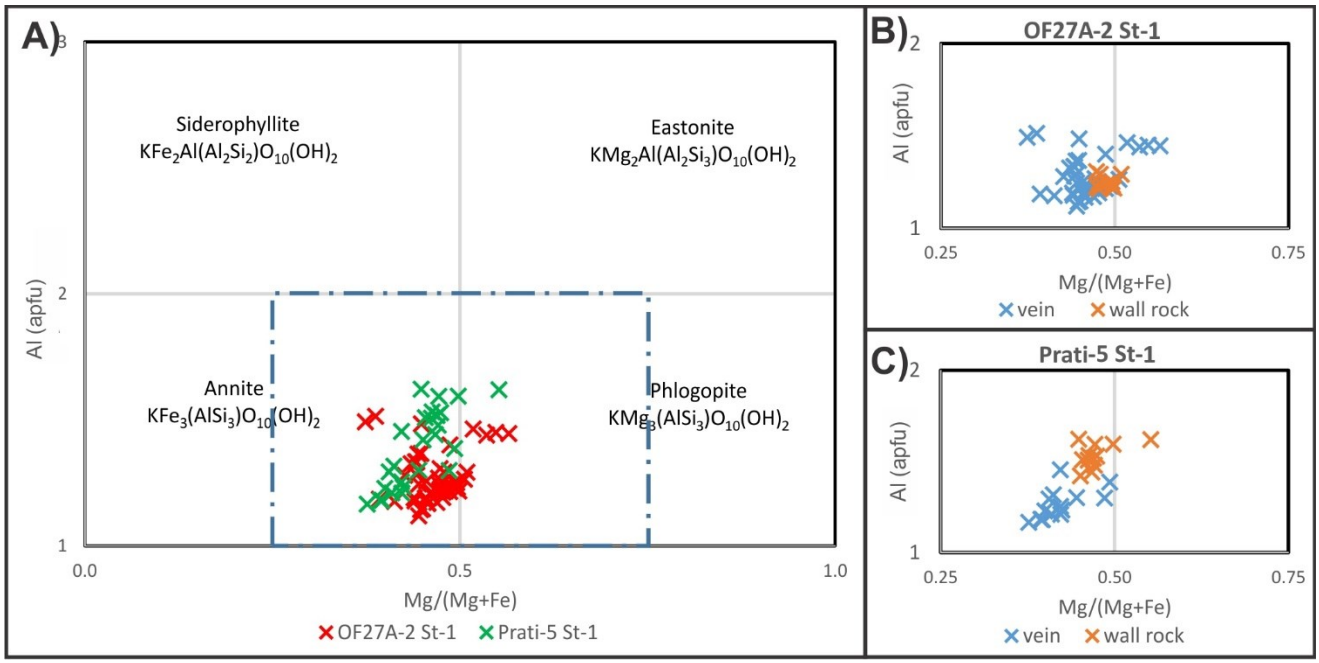

Figure 4: A) Biotite compositions from OF27A-2 St-1 and Prati-5 St-1. In B and C the compositions of vein and wall rock biotite are compared. The dashed blue area outlined in A in is the compositional space shown in B and C.

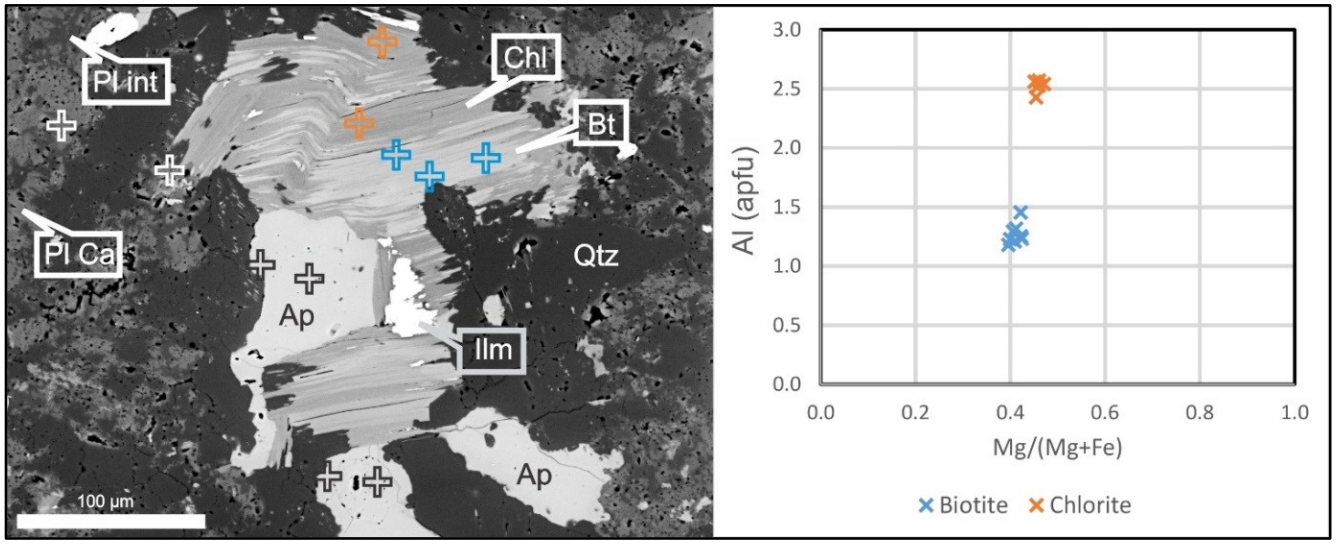

Figure 5: SEM BSE image of a biotite (Bt), apatite (Ap), quartz (Qtz) and ilmenite (Ilm) vein with a plagioclase (Pl) vein selvage from Prati-5 St-1 9940.28 ft. Biotite (lighter gray in BSE) has been partially replaced by chlorite (darker gray). Chlorite is enriched in Mg/(Mg+Fe) and Al compared to the biotite it replaces. The compositional differences in the vein selvage plagioclase are reflected in the value of the grayscale in the BSE image. Ca-rich plagioclase (Pl Ca) has a brighter BSE grayscale than the more intermediate plagioclase (Pl Int), with quartz as the darkest phase in the image.

3.1.2 Tourmaline

Tourmaline has a general formula of $XY_3Z_6(T_6O_{18})(BO_3)_3V_3W$, with sites in analyzed tourmaline from The Geysers occupied as follows: X = Na^{1+}, □ (vacancy), K^{1+}, Ca^{2+}; Y = Fe^{2+}, Mg^{2+}, Al^{3+}, Ti^{4+}, Mn^{2+}; Z = Al^{3+}, Mg^{2+}; T = Si^{4+}, Al^{3+}; B = B^{3+}; V = OH^{1-}, W = OH^{1-}, F^{1-}, O^{2-}, Cl^{1-}.

The EMP data was normalized to fifteen cations in the Y+Z+T sites for the calculation of structural formulas. This normalization procedure is considered appropriate for nearly all metamorphic tourmaline (Henry et al., 2011).The following assumptions were made when calculating chemical formulas: no vacancies in the T+Z+Y sites; B sites are filled by B; and OH is the dominant anion in the V sites. Estimates of OH and O in the W site were made by putting all measured F and Cl in that site and selecting a ratio of OH to O that would charge balance the structural formula. Tourmaline classification graphs are presented in figure 6 using the classification schemes and nomenclature of Henry et al. (2011). These graphs show ternary diagrams of the X-site (Ca vs Na+K vs vacant) and W-site (O vs OH vs F) as well as graphs showing generalized tourmaline groups appropriate for alkaline and X-site vacant dominant tourmalines. Although calculations of the W-site occupancy have been made, without complete chemical analyses theses estimates have proven to be unreliable (Henry et al., 2011) and therefore generalized tourmaline species names are used. Raw EMP data and calculated formulas of representative tourmaline analyses can be found in the appendix.

One hundred and sixteen EMP analyses of tourmaline have been collected for this study. In addition, Calpine made eleven legacy analyses available. Tourmaline was observed in veins within the felsite and biotite hornfels, and in the biotite hornfels wall rock. Figure 6 illustrates the data from thirty-two analyses from DV-2 (vein), twenty-one from OF27A-2 St-1(six vein, fifteen wall rock and eleven legacy analyses), sixty-two from GDC-30 (vein) and two from DV-2 (vein).

Vein tourmaline from DV-2 forms euhedral and elongate radiating crystals with tourmaline precipitating prior to chlorite, quartz, K-feldspar, epidote and titanite. In cross-sections perpendicular to the C-axis tourmaline often shows zoning in SEM BSE imaging with darker cores and narrow lighter rims, however the rims were too thin for EMP analysis. In BSE imaging it is common to see the lighter BSE rims preserved with interiors replaced by the encapsulating K-feldspar and less commonly quartz. Perpendicular to the C-axis the elongate tourmaline crystals show zoning from base to tip in Mg, Fe, Al and X-site vacancy, with terminations enriched in Fe and depleted in Mg, Al and X-site vacancies relative to the base of the crystal (Figure 7). Average values of base and tips are (in apfu): 0.27 and 0.04 for Mg/(Mg+Fe); 6.65 and 7.01 for total Al; and 0.32 and 0.57 for X-site vacancies. Norton and Dutrow (2001) reported similar trends and values in tourmalines zoned from core to rim in DV-2.

Tourmaline from OF27A-2 St-1 has two morphologies, large euhedral to subhedral zoned tourmaline in the biotite hornfels wall rock and acicular radiating crystals within the veins (Figure 8). The zoned wall rock tourmaline often contains bright BSE bands that can cut concentric zones, indicating a period of dissolution. Vein tourmaline occurs with epidote, K-feldspar, plagioclase, quartz, chalcopyrite, pyrite and titanite with tourmaline precipitating first. By comparison vein tourmaline is enriched in Al and F and is more prone to contain vacancies at the X-site, and wall rock tourmaline is enriched in Mg and Ca. Average values for vein tourmaline are as follows (in apfu): Mg/(Mg+Fe) = 0.34; Al = 6.57; F = 0.20; □ = 0.30, Mg = 0.84; and Ca = 0.17. Average values for wall rock tourmalines are as follows (in apfu): Mg/(Mg+Fe) = .42; Al = 5.79; F = 0.03; □ = 0.11; Mg = 1.32; and Ca = 0.31.

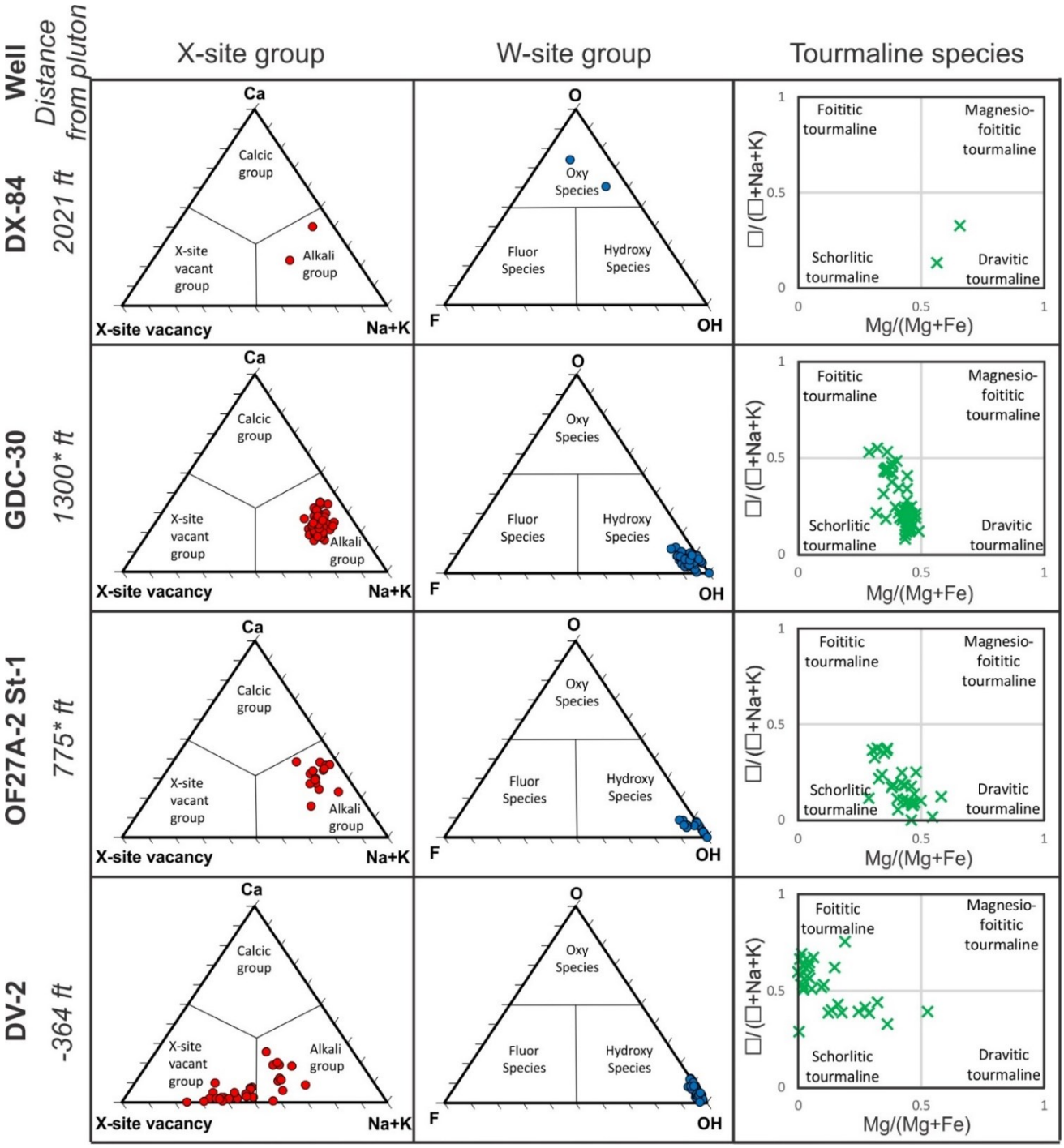

Figure 6: Tourmaline classifications by well based on atoms per formula unit values calculated from EMP analyses. Wells are organized by distance from the intrusive in feet (*exact distances from the pluton to cores OF27A-2 St-1 and GDC-30 are not known). X-sites can be filled by Ca, Na, K or are vacant (□). After assigning F to the W site sufficient O and OH were added to achieve a neutral charge balance. The generalized tourmaline species of Henry et al. (2011) were used that are appropriate for alkali and/or x-site dominant tourmaline with (Mg+Fe)/(Mg+Fe+2Li) > 0.5 and EMP data without H_2O analyses.

GDC-30 contains abundant large (100s of µm) zoned tourmaline crystals in veins and vein selvages where it precipitated prior to chlorite and quartz. Tourmaline displays oscillatory zoning from core to rim as well as sector zoning. In addition, slender late tourmaline growths on the C+ pole are observed in grains oriented appropriately. The oscillatory zoning goes through the sector zones but not the late C^+ overgrowths. The center of oscillatory zoning is often at or near the vein wall and quartz inclusions in the tourmaline of the vein selvages are common. These tourmaline crystals may have nucleated on detrital tourmaline grains in the fine-grained metasediment of the Franciscan Complex wall rock. The sector zones and late C^+ overgrowths have different pleochroic color patterns in thin section: C domains = brown to blue; A domains = shades of brown; and C^+ overgrowths = shades of blue (Figure 9). In SEM

BSE imaging the A domains are lighter shades of gray, and the C domains are darker (Figure 10). The A domains are enriched in Ca, Ti, Mg, Na, F and Si. The C domains are enriched in Al and contain more X-site vacancies. Two possible substitutions to account for the chemical variation between the A and C domains are $(Al^{+3})^{Y} + (Al^{+3})^{Z} = (Ti^{+4})^{Y} + (Mg^{+2})^{Z}$ and $(Al^{+3})^{YorZ} + (\square)^{X} = (Mg^{+2})^{YorZ} + (Ca)^{X}$. Average values for the A domains are as follows (in apfu): Mg/(Mg+Fe) = 0.44; Al = 5.88; Mg = 1.32; Ti = 0.17, □ = 0.14, F = 0.23 and Ca = 0.24. Average values for the C domains are as follows (in apfu): Mg/(Mg+Fe) = 0.38; Al = 6.55; Mg = 0.90; Ti = 0.04, □ = 0.42, F = 0.05 and Ca = 0.05.

Tourmaline from DX-84 occurs in veins with epidote, quartz, K-feldspar and chlorite. In these veins, tourmaline precipitated prior to quartz and epidote with later K-feldspar and chlorite. The tourmaline crystals in the veins form acicular masses of radiating needles. Due of their small size only two of the twelve EMP analyses were usable. The poor analyses had high Al, K and Si indicating K-feldspar contamination, which is the dominant encapsulating phase. Like the tourmaline in DV-2 the vein tourmalines showed narrow rims with brighter BSE grayscale values than the cores, but the rims are too narrow to analyze by EMP. The tourmaline from DX-84 differ from the other cores in that they are the only oxy species observed with O (calculated) as the dominant anion at the W-site, and are Mg-rich (dravitic) compared to other tourmaline analyzed.

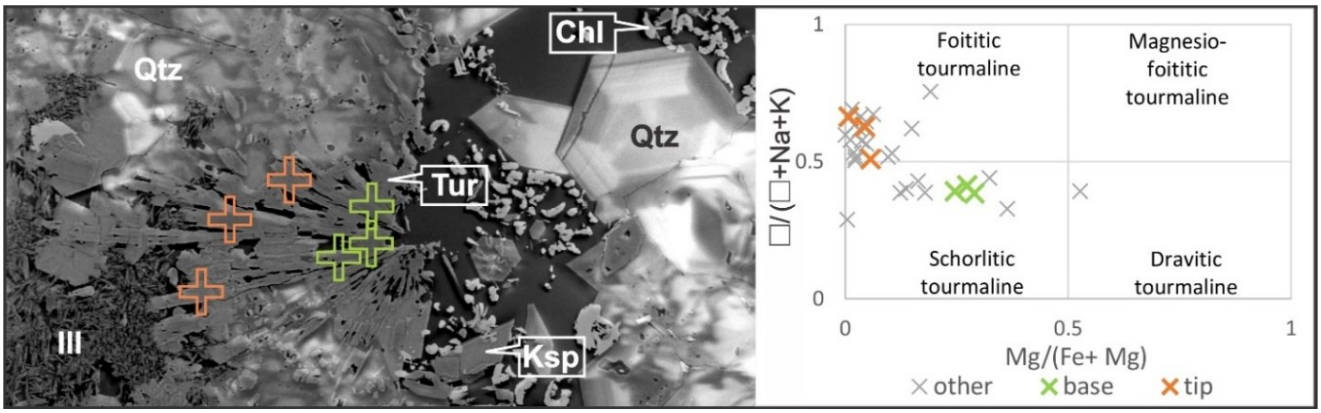

Figure 7: A partially transparent CL SEM image is overlain on a BSE SEM image of a tourmaline (Tur), quartz (Qtz), K-feldspar (Ksp) and chlorite (Chl) vein from DV-2. Tourmaline forms the radiating spray of crystals on the left hand side of the image with EMP points shown by hollow crosses. Also shown are CL zoned quartz in the vein (black annotation on right) and wall rock (white annotation on left). Tourmaline shows zoning parallel to the C-axis from the base (green crosses) to tip (orange crosses) in the elongated crystals growing into the wall rock.

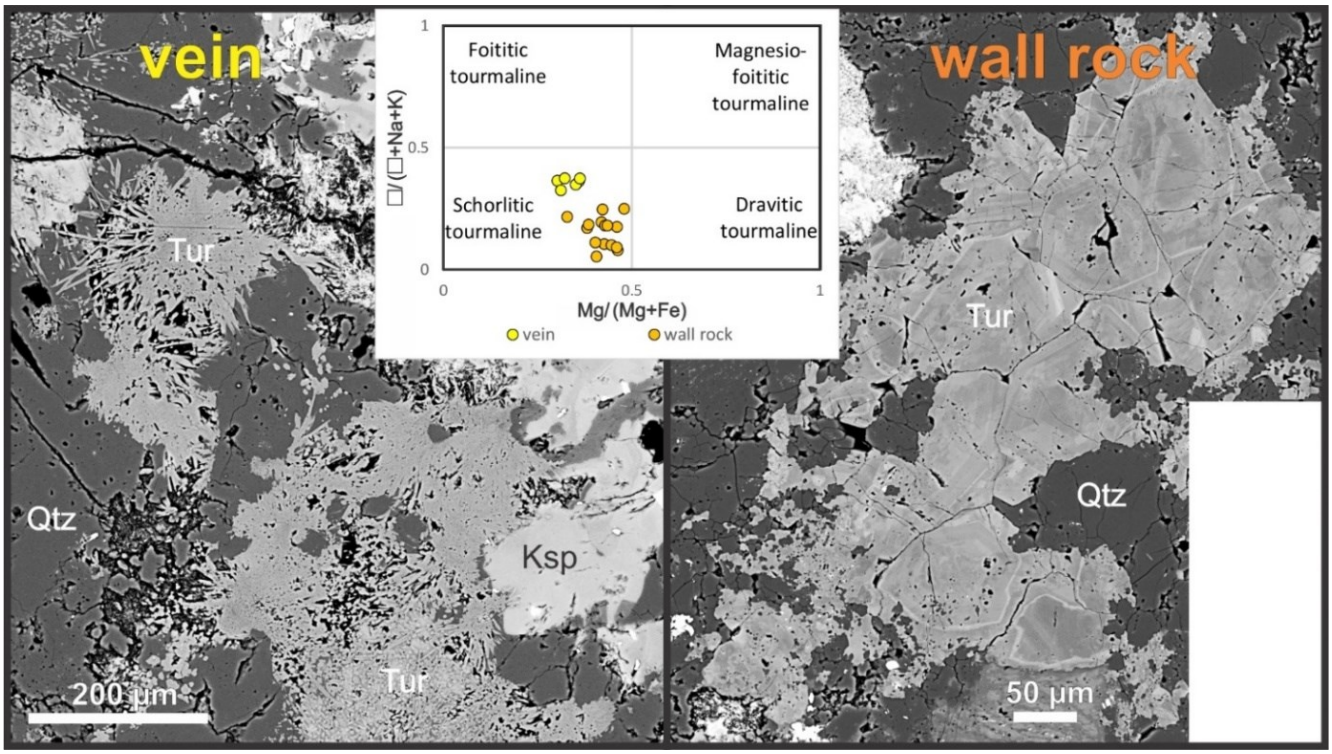

Figure 8: BSE SEM images of vein (left) and wall rock (right) tourmaline from OF27A-2 St-1. Vein tourmaline consists of acicular needles encapsulated by quartz and K-feldspar. Wall rock tourmaline contains bright BSE zones that may cut

oscillatory growth zones and is interpreted as a dissolution texture (best seen in the lower portion of the right hand image immediately above the scale bar).

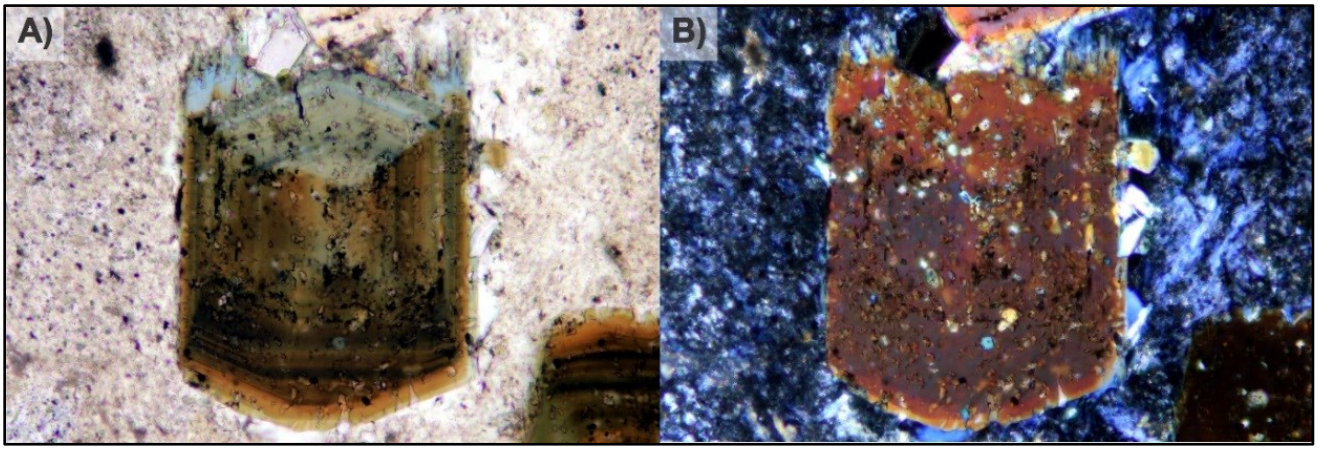

Figure 9: Photomicrographs of oscillatory and sector zoned tourmaline from GDC-30 with late stage tourmaline overgrowths growths on the C^{+} axis (top of image). The C domain is pleochroic from blue to brown (top of crystal, best observed in A). The A domain is pleochroic in shades of brown. The C^{+} over growths are pleochroic in shades of blue. Field of view = 0.6 mm. A) Plane polarized light. B) Crossed polarized light.

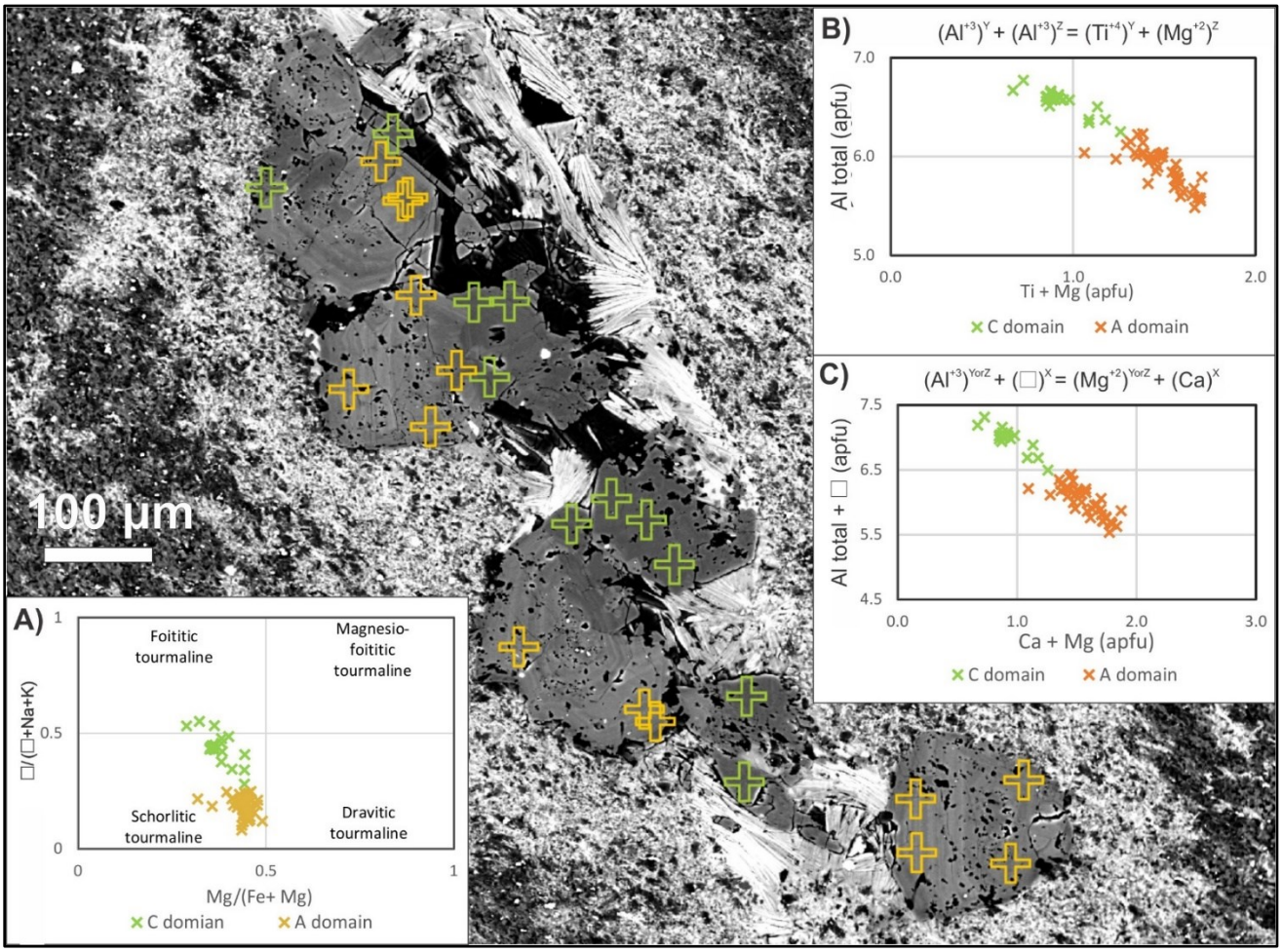

Figure 10: BSE SEM image of oscillatory and sector zoning in vein tourmaline from GDC-30. The vein also contains chlorite (light gray to white) and quartz (black), as well as a chlorite-rich vein selvage. Crosses indicate EMP measurement points of the C (green) and the A (orange) domains (not all points shown in graphs are on the image). A) Comparison of the A and the C domains. B & C) Possible exchange vectors between the A and C domains.

3.1.3 Calcic amphibole (actinolite)

Twenty EMP analyses of calcic amphibole were collected from Prati-5 St-1 9941.86 ft. The general formula for a calcic amphibole is $AB_2C_5T_8O_{22}(OH)_2$ with sites filled as follows: A = □ (vacancy)>Na^{1+}, K^{1+}; B = Ca^{2+}>Fe^{2+}>Mn^{2+} and Na^{1+}; C = Mg^{2+}, Fe^{2+}> Al^{3+} > Fe^{3+} and T^{4+} = Si^{4+} > Al^{3} .Calcic amphibole was observed in DX-84 and Prati-5 St-1. In DX-84 it occurs in veins as tiny inclusions in quartz with epidote and chlorite that were too small to analyze by EMP. In Prati-5 St-1, calcic amphibole occurs with apatite, quartz and pyrite within veins with Ca-rich plagioclase vein selvages. Formulas were calculated for calcic amphiboles using the methods presented in Leake et al. (1997), including Fe^{2+}/Fe^{3+} calculations, site assignments and the determinations of mineral species. Calcic amphiboles from The Geysers plot in the actinolite and magnesiohornblende fields (Figure 11). Average F and Cl contents of calcic amphibole are 0.01 and 0.08 apfu respectively. Raw EMP data and calculated formulas of representative calcic amphibole analyses can be found in the appendix.

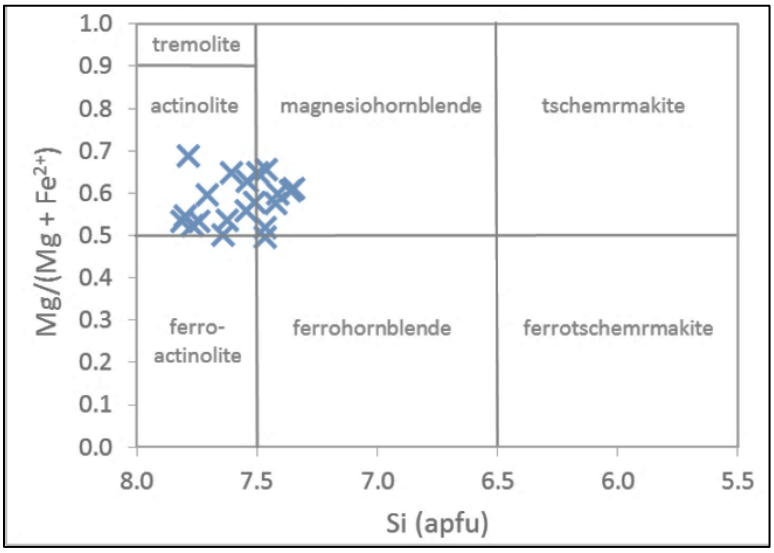

Figure 11: Classification of the calcic amphiboles found in veins from Prati-5 St-1 9941.86 ft based on chemical formulas calculated from EMP data. Diagram parameters: Ca in B site > 1.5 apfu; and Na + K at A site < 0.5 apfu (Leake et al., 1997).

3.1.4 Apatite

Thirty-three EMP analyses of apatite were collected from biotite- and calcic amphibole-bearing veins in OF27A-2 St-1 and Prati-5 St-1 cores. Apatite formulas were calculated from EMP data based on the methods of Ketcham et al. (2015). In an attempt to minimize F migration under the electron beam F was analyzed first. Notable differences in the F and Cl content of apatite were observed between OF27A-2 St-1 and Prati-5 St-1 (Figure 12). There was no F detected in Prati-5 St-1, but minor variations in Cl and OH (calculated) were observed. OF27A-2 St-1 contains little Cl (max 0.07 apfu), but had quite variable F and OH (calculated). These variations in F content in OF27A-2 St-1 were apparent at the grain scale with values ranging from 1.83 to 0 apfu in a single crystal. Raw EMP data and calculated formulas of representative apatite analyses can be found in the appendix.

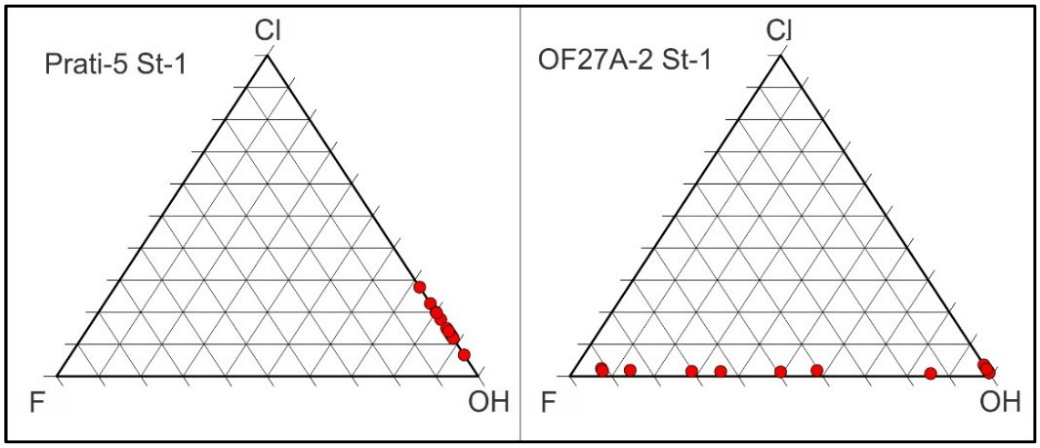

Figure 12: Ternary diagrams of the F, Cl and OH abundances on the monovalent anion sites of apatite based on formulas calculated from EMP data from wells Prati-5 St-1 and OF27A-2 St-1. Apatite from Prati-5 occurs in veins and plagioclase vein selvages with calcic amphibole, biotite, quartz and pyrite, and is variable in Cl and OH with no F detected. Apatite from OF27A-2 St-1 occurs in veins with biotite, quartz and pyrite, and is variable in F and OH at the grain scale and contains minor Cl.

3.1.5 Plagioclase

Fourteen EMP analyses of the plagioclase vein selvages in Prati-5 St-1 were collected. Calculation of plagioclase chemical formulas from EMP data were made by normalizing on eight oxygens. The plagioclase of the vein selvages is generally Ca-rich with an average composition of An_{75} (Figure 13). However, the vein selvages have a patchy texture in BSE imaging, and EDS analyses showed that they are dominated by lighter (BSE grayscale) Ca-rich areas with less abundant, darker areas of intermediate plagioclase (Figure 4). Raw EMP data and a calculated formula of a representative plagioclase analysis can be found in the appendix.

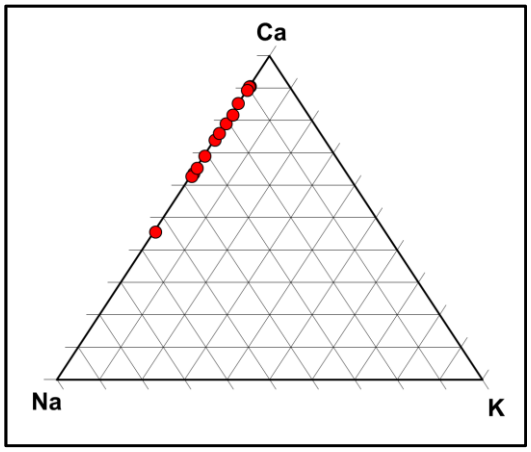

Figure 13: Plagioclase chemical data calculated from EMP analyses of the plagioclase vein selvages in Prati-5 St-1.

3.1.6 Chlorite

Forty-three EMP analyses of chlorite were collected from: DV-2 (eleven) where it precipitates in veins with tourmaline, K-feldspar, quartz, epidote and titanite; GDC-30 (twenty) where it precipitates in veins with tourmaline and quartz; OF27A-2 St-1 (one) where it precipitates with tourmaline, K-feldspar, plagioclase, quartz, chalcopyrite, pyrite and ilmenite; DX-84 (six) where it precipitates with tourmaline, epidote, K-feldspar, and quartz; and Prati-5 St-1 (five) where it is an alteration product of biotite. Structural formulas where calculated from EMP data based on fourteen oxygens per formula unit. Chlorite plots primarily in the clinochlore field with less common chamosite (Figure 15). Chlorite shows a trend of increasing Mg content away from the pluton (Figure 15). Chlorite replacements of biotite in Prati-5 St-1 are enriched in Mg and Al compared to coexisting biotite (Figure 4). Raw EMP data and calculated formulas of representative chlorite analyses can be found in the appendix.

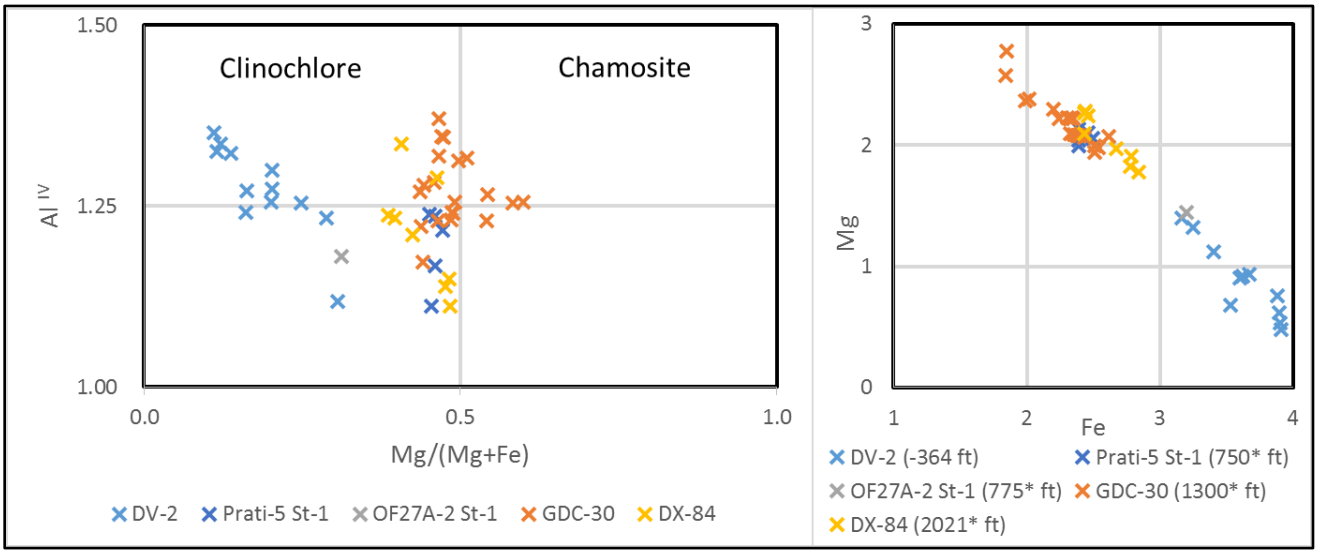

Figure 15: EMP data from vein chlorite (DV-2, GDC-30, OF27A-2 St-1 and DX-84) and secondary chlorite after biotite (Prati-5 St-1). Vein chlorite from within the intrusive is enriched in Fe compared to vein chlorite from the biotite hornfels (distances from the intrusive contact in feet are listed in the legend of the right hand figure, with * indicating that distances are uncertain). Elements plotted in atoms per formula unit.

3.1.7 K-feldspar

Twenty-five EMP analyses of K-feldspar were collected from: DV-2 (seventeen) where it precipitated in veins with tourmaline, chlorite, quartz, titanite and epidote; OF27A-2 St-1 (six) where it precipitated in veins with tourmaline, plagioclase, quartz, chlorite, chalcopyrite, pyrite, titanite and ilmenite; and DX-84 (two) where it precipitated in veins with tourmaline, chlorite, epidote and quartz. Chemical formulas were calculated on the basis of eight oxygens per formula unit. K was the dominant cation in all three wells with

minor Na (0.01 to 0.04 apfu in DV-2; 0.06 to 0.07 apfu in OF27A-2 St-1; and 0.04 apfu in DX-84), Ba (0.00 to 0.01 in DV-2; 0.1 to 0.03 apfu in OF27A-2 St-1; and 0.01 apfu in DX-84), and F (0.00 to 0.02 apfu in DV-2). Intermittent low values of Mg and Fe were also observed (≤0.01 apfu). Raw EMP data and calculated formulas of representative K-feldspar analyses can be found in the appendix.

3.2 Paragenesis 2

Cross cutting relationships observed demonstrate that veins containing epidote + quartz + K-feldspar + plagioclase ± actinolite ± chlorite ± chalcopyrite ± pyrite ± ilmenite ± prehnite ± wairakite; and K-feldspar ± pyrite ± titanite formed later than those of paragenesis 1.

3.2.1 Epidote

Thirty-one EMP analyses of epidote were obtained from DV-2 (nineteen) and DX-84 (twelve). Epidote formulas were calculated on the basis of twelve and a half oxygens per formula unit, with all iron assumed to be Fe^{3+}. Epidote was observed in DV-2 as a late stage mineral with titanite; in DX-84 it precipitated primarily in veins with chlorite and in a cross-cutting vein with tourmaline, K-feldspar, chlorite and quartz. In DV-2 epidote contained low abundances of rare earth elements (Ce < 0.17, Nd < 0.06, La < 0.11 apfu) and F (< 0.05 apfu). There appears to be no correlation in Fe^{3+} and Al content and proximity to the intrusive (DV-2 is within the pluton, DX-84 is 2021 ft from the pluton). Raw EMP data and calculated formulas of representative epidote analyses can be found in the appendix.

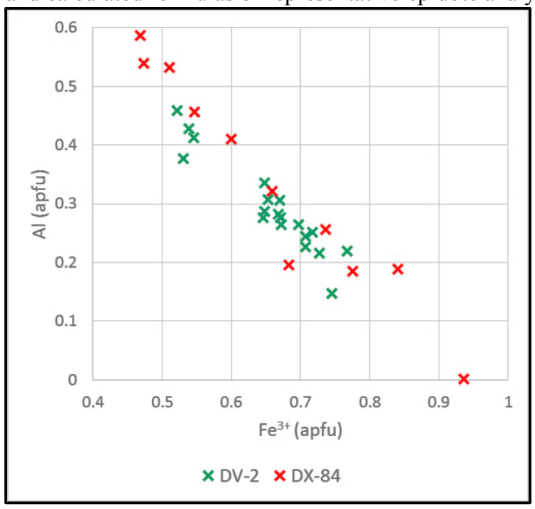

Figure 14: EMP data from vein epidote in DV-2 and DX-84.

3.2.2 Titanite

Eight EMP analyses of vein titanite were collected from the DV-2 core (seven) where it precipitated in veins with quartz, K-feldspar, epidote and chlorite, and OF27A-2 St-1 (one) where it precipitated in veins with K-feldspar and pyrite. Chemical formulas were calculated from electron microprobe data following the methods of Oberti et al. (1991), based on two cations per formula unit with the assumptions that all iron present is Fe^{3+} and that the tetrahedral and octahedral sites (Si, Ti, Al and Fe+3) contain no vacancies. Titanite deviated from the idealized structural formula of $CaSiTiO_5$ in that they contained Al and F and have an average formula (DV-2) of $Ca_{0.96}Si_{1.02}Ti_{0.60}Al_{0.39}Fe^{+3}_{0.01}O_{4.77}(F_{0.27}OH_{0.18})$. Al ranged from 0.35 to 0.41 with an average of 0.39 apfu in DV-2, and contained 0.21 apfu Al in OF27A-2 St-1. F ranged from 0.21 to 0.35 with an average of 0.27 apfu in DV-2, and OF27A-2 St-1 contained 0.11 apfu. Ba (≤0.01 apfu) and Fe^{3+} (≤0.03) were also detected in low abundances in some samples. A likely substitution would be $(Al, Fe)^{+3} + (F, OH)^{-} = T^{+4}$ (Enami et al., 1993; Figure 16). F generally accounts for > 50% of the substitution needed to charge balance the formula. OH values are calculated to make up the charge deficiency. Raw EMP data and a calculated formula of a representative titanite analysis can be found in the appendix.

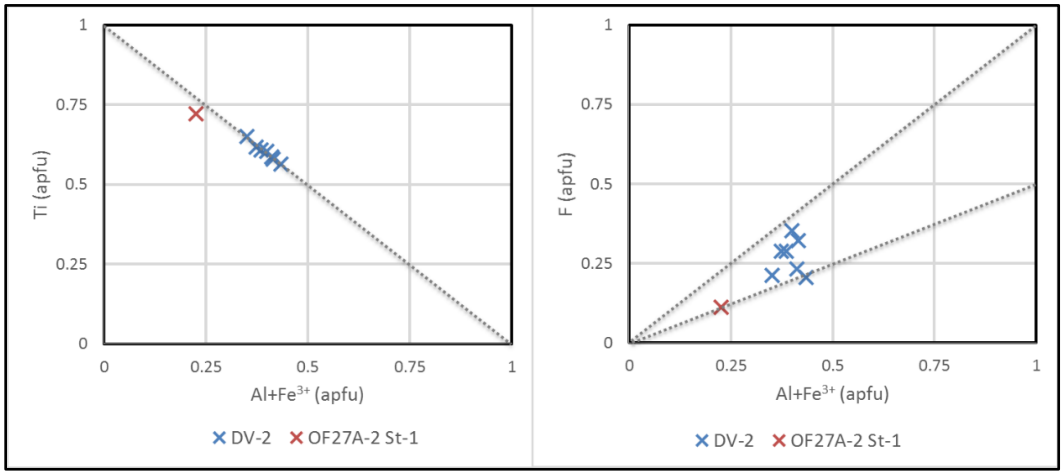

Figure 16: Vein titanite EMP data from DV-2 and OF27A-2 St-1 cores. The right hand image shows a substitution vector for Al and Fe replacing Ti. The left hand image shows that OH (not analyzed) must also be present for charge balance.

4. SUMMARY

Biotite from OF27A-2 St-1 and Prati-5 St-1 cores have similar compositions and are dominantly annite in composition with less abundant phologopite. Minor variations in Al, Mg/(Mg+Fe), Cl and F content were noted between vein biotite and biotite in the contact metamorphosed wall rock. However, biotite in Prati-5 St-1 is notably depleted in F compared to OF27A-2 St-1.

Foititc, scholitic and dravitic tourmaline species were observed in core samples from the felsite and biotite hornfels with foititic and schorlitic species being the most common. X-sites are dominated by Na and vacancies, and are therefore primarily members of the alkali group with less common X-site vacant group species. X-site vacant species are found primarily within the felsite in DV-2 and are Al-rich and Mg-poor. Calculated tourmaline W-site groups plotted almost exclusively in the hydroxy species field with rare oxy species from DX-84. No appreciable Cl was detected (≤0.01 apfu) in tourmaline. F in tourmaline does not have a systematic relationship with distance from the intrusion, with averages values (in apfu) of 0.04 in DV-2, 0.06 in OF27A-2 St-1, 0.17 in GDC-30 and 0.08 in DX-84 (listed in distance from intrusion). However, notable differences in F content were observed: between wall rock and vein tourmaline in OF27A-2 St-1 with average F contents of 0.03 apfu and 0.20 apfu respectively; and at the grain scale in the sector zoned tourmalines in GDC-30 with average F (in apfu) of 0.05 in the C domains and 0.25 in the A domains.

Calcic amphiboles from Prati-5 St-1 plot in the actinolite and magnesiohornblende fields and contain minor Cl (average 0.08 apfu) and negligible F (average 0.01 apfu). Apatite chemistry was variable between wells and at the grain scale. OF27A-2 St-1 contained nearly end member F and OH apatite species with large heterogeneities at the grain scale. Apatite from Prati-5 St-1 contains negligible F and is OH-rich with minor Cl (0.26 apfu). Plagioclase vein selvages from Prati-5 St-1 are Ca-rich with an average composition of An_{75}, however they contain a patchy texture in BSE imaging, and EDS analyses showed that they are dominated by lighter BSE grayscale value Ca-rich areas with less abundant, darker areas of intermediate plagioclase. No systematic zoning of Al and Fe^{+3} in epidote was observed with distance from the felsite. Epidote from veins within the intrusive in DV-2 contained low abundances of rare earth elements (Ce < 0.17, Nd < 0.06, La < 0.11 apfu). Chlorite was observed in veins from within the felsite out into the high temperature vapor dominated reservoir with Fe-rich chlorite in the felsite core from DV-2 (average Mg/(Mg+Fe) = 0.19) to more Mg-rich chlorite in the biotite hornfels (average Mg/(Mg+Fe) = 0.47). Titanite from veins in the felsite and biotite hornfels is enriched in Al and F. Vein K-feldspar contains low abundances of Na (0.01 to 0.07 apfu) and Ba (≤0.03 apfu).

Mineral chemistries from Prati-5 St-1 were notable in that they contained negligible F in analyses of apatite, biotite and calcic amphibole. F was observed in biotite, tourmaline, titanite, apatite, epidote and chlorite in the other core samples. F and Cl in the hydrothermal alteration minerals within the pluton and the contact metamorphosed country rock suggest that there may have been a magmatic contribution to the early hydrothermal system at The Geysers.

REFERENCES

Bufe, C. G., Marks, S. M., Lester, F. W., Ludwin, R. S. and Stickney, M. C. (1981). Seismicity of The Geysers-Clear Lake region. In: McLaughlin, R. J., Donnelly-Nolan, J. M. (Eds.), Research in The Geysers-Clear Lake Geothermal Area, Northern California. USGS Professional Paper 1141, 129-137.

Dalrymple, G. B., Grove, M., Lovera, O. M., Harrison, T. M., Hulen, J. B. and Lanphere, M. A. (1999). Age and thermal history of the Geysers plutonic complex (felsite unit); Geysers geothermal field, California. *Earth and Planetary Science Letters*, 173, 285-298.

Donnelly-Nolan, J. M., Burns, M. G., Goff, F. E., Peters, E. K. and Thompson, J. M. (1993). The Geysers-Clear Lake area, California: Thermal waters, mineralization, volcanism and geothermal potential. *Economic Geology*, 88, 301-316.

Donnelly-Nolan, J. M., Hearn, B. C. Jr., Curtis, G. H. and Drake, R. E. (1981). Geochronology and evolution of the Clear-Lake volcanics. In: McLaughlin, R. J., Donnelly-Nolan J. M. (Eds), Research in The Geysers-Clear Lake Geothermal Area, Northern California. USGS Professional Paper 1141, 47-60.

Drenick, A. (1986). Pressure-temperature, spinner survey in a well at The Geysers. *Proceedings of the 11th Workshop on Geothermal Reservoir Engineering*, Stanford University, CA, 197-206.

Enami, M., Suzuki, K., Liou, J. G., and Bird, D. K. (1993). Al-Fe3+ and F-OH substitutions in titanite and constraints on their PT dependence. *European Journal of Mineralogy*, 5(2), 219-231.

Henry, D. J., Novák, M., Hawthorne, F. C., Ertl, A., Dutrow, B. L., Uher, P., and Pezzotta, F. (2011). Nomenclature of the tourmaline-supergroup minerals. *American Mineralogist*, 96(5-6), 895-913.

Henry, D. J., and Dutrow, B. L. (1996). Metamorphic tourmaline and its petrologic applications. *Reviews in Mineralogy and Geochemistry*, 33(1), 503-557.

Hulen, J. B. (1991).Petrographic summaries for core from 15 geothermal wells in The Geysers steam field, California. University of Utah Research Institute report, 72.

Hulen, J. B., Walters, M. A. and Neilson, D. L. (1991). Comparison of reservoir and cap-rock core from the northwest Geysers steam field, California. *Geothermal Resources Council Transactions*, 15, 11-18.

Hulen, J. B., Neilson, D. L. and Martin, W., 1992. Early calcite dissolution as a major control on porosity development in The Geysers steam field, California – additional evidence from Unocal well NEGU-17. *Geothermal Resources Council Transactions*, 16, 167-174.

Hulen, J. B., Heizler, M.T., Stimac. J. A., Moore, J. N. and Quick, J. C. (1997). New constraints on the timing of magmatism, volcanism and the onset of vapor-dominated conditions at The Geysers steam field, California. *Proceedings of the 22nd Workshop on Geothermal Reservoir Engineering*, Stanford University, CA. 75-82.

Hulen, J. B. and Norton, D. L. (2000). Wrench-fault tectonics and emplacement of The Geysers felsite. *Geothermal Resource Council Transactions,* 24, 24-27.

Isherwood, W. F. (1981) Geophysical overview of The Geysers. McLaughlin, R. J. and Donnelly-Nolan J. M. (Eds), *Research in The Geysers-Clear Lake Geothermal Area, Northern California*. USGS Professional Paper 1141, 83-95.

Kennedy, B. M. and Truesdell, A. H. (1996). The Northwest Geysers high-temperature reservoir: evidence for acting magmatic degassing and implications for the origin of The Geysers Geothermal field. *Geothermics*, 25(3), 365-387.

Ketcham, R. A. (2015) Technical Note: Calculation of stoichiometry from EMP data for apaite and other phases with mixing on monovalent anion sites. *American Mineralogist*, 100(7), 1620-1623.

Leake, B. F., Woolley, A. R., Arps, C. E. S., Birch, W. D., Grice, J. D., Hawthorne, F. C., Kato, A., Kisch, H. J., Krivovichev, V. G., Linthout, K., Laird, J., Mandarino, J. A., Maresch, W. V., Nickel, E. H., Schumacher, J. C., Nicholas C.N. Stephenson, N. C. N., Whittaker, E. J. W., and Youzhi, G. (1997). Nomenclature of amphiboles: report of the subcommittee on amphiboles of the International Mineralogical Association, Commission on New Minerals and Mineral Names. *The Canadian Mineralogist*, 35(1), 219-246.

Lowenstern, J. B. and Janik, C. J. (2003). The origins of reservoir liquids and vapors from The Geysers geothermal field. *Society of Economic Geologists Special Publication,* 10, 181-195.

Lutz S. J., Walters, M., Pistone, S., and Moore, J. N. (2012). New insights into the high-temperature reservoir, Northwest Geysers. Geothermal Research Council Transactions 36, 907-916.

McLaughlin, R. J. (1981). Tectonic setting of pre-Tertiary rocks and its relation to geothermal resources in the Geysers-Clear Lake area. McLaughlin, R. J., Donnelly-Nolan J. M. (Eds), Research in The Geysers-Clear Lake Geothermal Area, Northern California. USGS Professional Paper 1141, 25-45.

McNitt, J. R. (1968). Geology of the Kelseyville quadrangle, Sonoma, Lake and Mendocino counties, California. California Division of Mines and Geology, Map Sheet 9.

Moore, J. N. and Gunderson, R. P. (1995). Fluid inclusion and isotopic systematics of an evolving magmatic-hydrothermal system. *Geochimica et Cosmochimica Acta*, 59(19), 3887-3907.

Moore, J. N., Adams, M. C., and Anderson, A. J. (2000). The fluid inclusion and mineralogic record of the transition from liquid- to vapor-dominated conditions in The Geysers geothermal system, California. Economic Geology 95, 1719-1737.

Moore, J. N. and Simmons, S. F. (2013). More power from below. *Science*, 340 (6135), 933-934.

Norton, D. L. and Hulen, J. B., (2001). Preliminary numerical analysis of the magma-hydrothermal history of The Geysers geothermal system, California. *Geothermics*, 30(2-3), 211-234.

Norton, D. L., & Dutrow, B. L. (2001). Complex behavior of magma-hydrothermal processes: role of supercritical fluid. *Geochimica et Cosmochimica Acta*, 65(21), 4009-4017.

Oberti, R., Smith, D. C., Rossi, G., and Caucia, F. (1991). The crystal-chemistry of high-aluminium titanites. *European Journal of Mineralogy*, 3(5), 777-792.

Oppenheimer, D. H. (1986). Extensional tectonics at The Geysers geothermal area, California. *Journal of Geophysical Research,* 91, 11,463-11,476.

Pulka, F. S. (1991). Subsurface geology at Ford Flat, Geysers geothermal system, California. M.S. Thesis. Houghton Michigan Tech.

Schmitt, A. K., Grove, M., Harrison, T. M., Lovera. O., Hulen, J. B. and Walters, M. (2002). Intrusion ages of The Geysers plutonic complex determined by ion microprobe U-Pb dating of zircon. *Geothermal Recourses Council Transactions*, 26, 22-25.

Schriener, A. Jr. and Suemnicht, G. A. 1981. Subsurface intrusive rocks at The Geysers geothermal area, California. In: Silberman, M. L., Field, C. W., Berry, A. L. (Eds.), *Proceedings of the symposium on mineral deposits of the Pacific Northwest*. USGS Open File Report, 81-355, 295-302.

Stanley, W. D. and Blakely, R. J. (1995). The Geysers-Clear Lake geothermal area, California – An updated geophysical perspective of heat sources. *Geothermics*, 24, 187-221.

Sternfeld, J. N. (1981). The hydrothermal petrology and stable isotope geochemistry of two wells in The Geysers geothermal field, Sonoma County, California. MS Thesis. University of California Riverside.

Sternfeld, J. N. (1989). Lithologic influences on fracture permeability and the distribution of steam in the Northwest Geysers steam field, Sonoma County, California. *Geothermal Resources Council Transactions*, 13, 473-479.

Thompson, R. C. (1989). Structural stratigraphy and intrusive rocks at The Geysers geothermal fields. *Geothermal Resource Council Transactions*, 13, 481-486.

Thompson, R. C. and Gunderson, R. P. (1989). The orientation of stem-bearing fractures at The Geysers geothermal Field. *Geothermal Resources Council Transaction*, 13, 481-485.

Torgensen, T. and Jenkins, W. J. (1982). Helium isotopes in geothermal systems: Iceland, The Geysers, Raft River, and Steamboat Springs. *Geochimica et Cosmochimica Acta*, 46, 739-748.

Truesdell, A. H. and White, D. E. (1973). Production of superheated steam from vapor-dominated geothermal reservoirs. *Geothermics*, 2, 154-173.

Truesdell, A., Haizlip, J. R., Armannsson, H. and D'Amore, F. (1989). Origins and transport of chloride in superheated geothermal steam. *Geothermics*, 18(1-2), 295-304.

Walters, M. and Combs, J., (1989). Heat flow in The Geysers-Clear lake area of Northern California, USA. *Geothermal Recourse Council Transactions*, 13, 491-502.

Walters, M., Haizlip, J. R., Sternfeld, J. N., Drenick, A. F. and Combs, J. (1988). A vapor-dominated reservoir exceeding 600^{o}F at The Geysers, Sonoma County California. *Proceedings of the 13th Workshop on Geothermal Reservoir Engineering*, Stanford University, CA, 73-81.

Walters, M. A. and Combs, J. (1992). Heat flow in The Geysers-Clear Lake geothermal area of northern California, USA. *Monograph on the Geysers Geothermal Field*, 43-53.

Williams, C. F., Galanis, S. P. Jr., Moses, T. H. Jr. and Grubb, F. V. (1993). Heat-flow studies in the northwest Geysers geothermal field, California. *Geothermal Recourse Council Transactions,* 17, 281-288.

White, D. E., Muffler, L. J. P., and Truesdell, A. H. (1971). Vapor-dominated hydrothermal systems compared with hot-water systems. *Economic Geology*, 66(1), 75-97.

APPENDIX

Representative EMP analyses and calculated structural formulas are provided in tables by mineral. Raw data is in weight percent oxide.

Biotite

Well	OF27A-2 St-1	OF27A-2 St-1	Prati-5 St-1	Prati-5 St-1
line #	4_Bt 7	WR_1 Bt3	9940.28 Bt7	9940.28 WRBt8
vein or wall rock	vein	wall rock	vein	wall rock
Al_2O_3	16.360	13.605	13.280	15.857
MgO	12.643	10.902	9.684	10.164
Na_2O	0.000	0.045	0.050	0.037
F	1.354	1.247	0.000	0.000
K_2O	9.525	9.686	9.353	9.406
CaO	0.047	0.000	0.000	0.022
FeO	17.353	21.304	23.420	20.662
SiO_2	38.050	36.652	36.065	36.495
Cl	0.132	1.695	2.471	1.270
MnO	0.073	0.083	0.131	0.088
TiO_2	1.399	2.266	2.630	2.034
Oxide Totals	96.978	97.483	97.174	96.129
H_2O (calc)	3.324	2.825	3.180	3.566
New Oxide Totals (calc)	100.281	100.310	100.265	99.599
Calculated formulas				
A-site				
K	0.91	0.96	0.94	0.93
Na	0.00	0.01	0.01	0.01
Ca	0.00	0.00	0.00	0.00
A-site total	0.91	0.97	0.95	0.93
Tetrahedral sites				
Si	2.85	2.86	2.84	2.81
Al IV	1.15	1.14	1.16	1.19
Tetrahedral sites total	4.00	4.00	4.00	4.00
Octahedral sites				
Fe	1.09	1.39	1.54	1.33
Mg	1.41	1.27	1.14	1.17
Al VI	0.30	0.11	0.07	0.26
Ti	0.08	0.13	0.16	0.12
Mn	0.00	0.01	0.01	0.01
Octahedral sites toatl	2.88	2.90	2.92	2.88
Hydroxyl sites				
OH	1.66	1.47	1.67	1.83
Cl	0.02	0.22	0.33	0.17
F	0.32	0.31	0.00	0.00
Hydroxyl sites total	2.00	2.00	2.00	2.00

Tourmaline

Well	DV-2	DV-2	OF27A-2 St-1	OF27A-2 St-1	GDC-30	GDC-30	DX-84
line #	6_T5	6_T7	2-T5-Rim	WR_1 Tur2	3_T9	4_T15	T4-wall
raw data (wt %)	base	tip	vein	wall rock	C-domain	A-domain	
Al_2O_3	32.836	35.978	29.725	29.909	33.916	28.950	31.770
MgO	2.504	0.350	5.668	4.459	3.406	5.382	7.021
Na_2O	1.456	1.109	1.754	1.779	1.394	2.042	1.607
F	0.219	0.012	0.000	0.000	0.214	0.301	0.000
K_2O	0.012	0.013	0.017	0.015	0.010	0.043	0.029
CaO	1.112	0.139	1.654	1.514	0.197	1.276	1.316
FeO	13.682	13.621	11.823	12.658	10.645	12.169	6.525
SiO_2	34.008	35.140	35.111	35.133	36.071	35.142	37.107
Cl	0.037	0.000	0.044	0.021	0.013	0.011	0.000
MnO	0.000	0.020	0.046	0.063	0.042	0.051	0.000
TiO_2	0.059	0.068	0.438	0.585	0.261	1.589	1.231
Oxide Totals	86.290	86.647	86.571	86.244	86.356	86.952	86.875
B_2O_3 (calc)	10.188	10.373	10.295	10.209	10.458	10.278	10.591
H_2O(calc)	3.116	3.108	3.291	3.104	3.117	3.039	2.922
Oxide Totals (calc)	99.757	100.293	100.081	99.477	100.009	100.424	100.194
Calculated formulas (apfu)							
X-site							
Na	0.48	0.36	0.57	0.59	0.67	0.45	0.51
K	0.00	0.00	0.00	0.00	0.01	0.00	0.01
Ca	0.20	0.02	0.30	0.28	0.23	0.04	0.23
X-site vacancy	0.31	0.61	0.12	0.13	0.09	0.51	0.25
X-site total	1.00	1.00	1.00	1.00	1.00	1.00	1.00
T-site							
Si	5.80	5.89	5.93	5.98	5.94	5.99	6.09
Al IV	0.20	0.11	0.07	0.02	0.06	0.01	0.00
T-site Total	6.00	6.00	6.00	6.00	6.00	6.00	6.09
Z-site							
Al VI	6.00	6.00	5.84	5.98	5.71	6.00	6.00
Mg	0.00	0.00	0.16	0.02	0.29	0.00	0.00
Z-site total	6.00	6.00	6.00	6.00	6.00	6.00	6.00
Y-site							
Fe	1.95	1.91	1.67	1.80	1.72	1.48	0.90
Mg	0.64	0.09	1.27	1.11	1.07	0.84	1.72
Al VI	0.40	0.99	0.00	0.00	0.00	0.64	0.15
Mn	0.00	0.00	0.01	0.01	0.01	0.01	0.00
Ti	0.01	0.01	0.06	0.07	0.20	0.03	0.15
Y-site total	3.00	3.00	3.00	3.00	3.00	3.00	2.91
B-site							
B	3.00	3.00	3.00	3.00	3.00	3.00	3.00
V-site							
OH	3.00	3.00	3.00	3.00	3.00	3.00	3.00
W-site							
OH	0.76	0.68	0.93	0.74	0.63	0.66	0.39
F	0.12	0.01	0.00	0.00	0.16	0.11	0.00
Cl	0.01	0.00	0.01	0.01	0.00	0.00	0.00
O	0.11	0.31	0.06	0.26	0.20	0.22	0.61
W-site total	1.00	1.00	1.00	1.00	1.00	1.00	1.00

Calcic Amphibole

Well	Prati-5 St-1
line #	9941.86_Act6
raw data (wt %)	
Al_2O_3	4.858
MgO	13.476
Na_2O	0.331
F	0.000
K_2O	1.327
CaO	10.490
FeO	16.671
SiO_2	49.891
Cl	0.456
MnO	0.249
TiO_2	0.314
Oxide Totals	98.146
H_2O(calc)	1.911
New Oxide Totals (calc)	100.057
Calculated formulas (apfu)	
T-site	
Si	7.36
Al IV	0.64
T-site total	8.00
C-site	
Al VI	0.20
Mg	2.96
Fe3+	0.13
Fe2+	1.67
Ti	0.03
C-site total	5.00
B-site	
Fe2+	0.26
Mn	0.05
Ca	1.66
Na	0.04
B-site total	1.96
A-site	
Na	0.06
K	0.25
A-site total	0.31
W-site	
F	0.00
Cl	0.11
OH	1.89
W-site total	2.00

Representative EMP Data and Calculated Formulas

Apatite

Well	OF27A-2 St-1	Prati-5 St-1
line #	Area 4_Ap 9	9941.86_Ap2
raw data (wt %)		
Al_2O_3	0.011	0.014
MgO	0.000	0.000
Na_2O	0.000	0.050
F	1.897	0.000
K_2O	0.031	0.000
CaO	53.975	54.160
FeO	0.177	0.161
SiO_2	0.050	0.000
Cl	0.100	0.959
MnO	0.000	0.000
TiO_2	0.057	0.034
P2O5	44.391	43.251
Oxide Totals	100.603	97.713
H_2O(calc)	0.900	1.553
New Oxide Totals (calc)	101.503	99.266
Calculated formulas (apfu)		
Ca	9.50	9.68
P	6.17	6.11
Na	0.00	0.02
K	0.01	0.00
Fe	0.02	0.02
Si	0.01	0.00
Ti	0.01	0.00
F	0.99	0.00
Cl	0.03	0.27
OH	0.99	1.73

Plagioclase

Well	Prati-5 St-1
line #	9940.28_An3
raw data (wt %)	
Al_2O_3	34.085
Na_2O	1.644
K_2O	0.015
CaO	17.144
FeO	0.055
SiO_2	46.386
Cl	0.046
Oxide Totals	99.364
Calculated formulas (apfu)	
Ca	0.85
Na	0.15
Al	1.86
Si	2.14

Epidote

Well	DV-2	DX-84
line #	9_E7	1-E4
raw data (wt %)		
Al_2O_3	25.98	27.46
MgO	0.01	0.02
Na_2O	0.01	-
F	-	-
K_2O	0.03	-
CaO	23.37	23.63
BaO	0.48	-
FeO	9.02	8.67
SiO_2	37.90	37.92
Cl	0.03	-
MnO	0.25	0.15
TiO_2	0.06	0.02
V_2O_3	0.04	
Ce_2O_3	0.11	
Nd_2O_3	-	
Nb_2O_5	-	
La_2O_3	0.06	
SrO		0.13
Oxide Totals	97.26	98.15
H_2O(calc)	1.77	1.81
New Oxide Totals (calc)	99.03	99.95
Calculated formulas (apfu)		
Ca	1.99	1.98
Sr	0.00	0.01
Ba	0.02	0.00
Al	2.43	2.53
Fe	0.54	0.51
Mn	0.02	0.01
Si	3.01	2.97

Representative EMP Data and Calculated Formulas

Chlorite

Well	DV-2	GDC-30	DX-84	Prati-5 St-1
line #	1_C4	4-C2	1-C2	9940.28_Chl1
raw data (wt %)				
Al_2O_3	20.10	20.605	19.59	19.47
MgO	3.60	14.143	11.25	12.63
Na_2O	0.00	0.020	0.00	0.00
F	0.07	0.072	0.00	0.00
K_2O	0.01	0.014	0.00	1.22
CaO	0.05	0.017	0.09	0.06
FeO	40.50	26.517	30.49	27.04
SiO_2	23.27	26.150	25.38	27.31
Cl	0.03	0.165	0.00	0.50
MnO	0.22	0.531	0.63	0.16
TiO_2	0.01	0.0235	0.00	0.59
Oxide Totals	88.14	88.55	87.89	89.02
H_2O(calc)	9.80	10.65	10.38	10.57
New Oxide Totals (calc)	97.93	99.20	98.26	99.60
Calculated formulas (apfu)				
Tetrahedral site				
Si	2.68	2.76	2.77	2.89
Al iv	1.32	1.24	1.23	1.11
Tetrahedral site total	4.00	4.00	4.00	4.00
Octahedral site				
Mg	0.62	2.22	1.83	1.99
Fe	3.90	2.34	2.78	2.39
Mn	0.02	0.05	0.06	0.01
Al vi	1.40	1.32	1.28	1.32
Ti	0.00	0.00	0.00	0.05
Octahedral site total	5.94	5.93	5.95	5.76
Monovalent anion site				
F	0.02	0.02	0.00	0.00
Cl	0.00	0.03	0.00	0.09
OH	7.97	7.95	8.00	7.91
Monovalent anion total	8.00	8.00	8.00	8.00

Titanite

Well	DV-2
line #	10_E5
raw data (wt %)	
Al_2O_3	10.825
MgO	0.022
Na_2O	0.043
F	3.142
K_2O	0.069
CaO	27.872
BaO	0.074
FeO	0.385
SiO_2	31.077
Cl	0.001
MnO	0.034
TiO_2	23.819
Oxide Totals	99.191
H_2O(calc)	0.695
New Oxide Totals (calc)	99.886
Calculated formulas (apfu)	
Ca	0.97
Si	1.00
Ti	0.58
Al	0.41
F	0.32
OH (calc)	0.16

K-feldspar

Well	DV-2	OF27A-2 St-1	DX-84
line #	8_K 5	3-K3	2-K4-INT
raw data (wt %)			
Al_2O_3	18.51	17.78	18.43
MgO	0.01	0.01	0.00
Na_2O	0.20	0.72	0.43
F	0.16	0.00	0.00
K_2O	16.64	15.40	16.14
CaO	0.00	0.00	0.00
BaO	0.02	1.49	0.35
FeO	0.06	0.15	0.11
SiO_2	65.24	63.39	63.59
Cl	0.00	0.00	0.02
Oxide Totals	100.80	99.05	99.10
Calculated formulas (apfu)			
Al	1.00	0.99	1.02
Na	0.02	0.07	0.04
F	0.02	0.00	0.00
K	0.98	0.93	0.97
Ba	0.00	0.03	0.01
Fe	0.00	0.01	0.00
Si	3.00	2.99	2.98